Optogenetic stimulation reveals a latent tipping point in cortical networks during ictogenesis

Robert T. Graham,[†] R. Ryley Parrish,[‡] Laura Alberio, Emily L. Johnson, Laura Owens and Andrew J. Trevelyan

Abstract

Brain state transitions are readily apparent from changes in brain rhythms[1], but are difficult to predict, suggestive that the underlying cause is latent to passive recording methods. Among the most important transitions, clinically, are the starts of seizures. We here show that an "active probing" approach may have several important benefits for epileptic management, including by helping predict these transitions. We used mice expressing the optogenetic actuator, channelrhodopsin, in pyramidal cells, allowing this population to be stimulated in isolation. Intermittent stimulation at frequencies as low as 0.033Hz (period = 30s) delayed the onset of seizure-like events in an acute brain slice model of ictogenesis, but the effect was lost if stimulation was delivered at even lower frequencies (1/min). Notably, active probing additionally provides advance indication of when seizure-like activity is imminent, revealed by monitoring the postsynaptic response to stimulation. The postsynaptic response, recorded extracellularly, showed an all-or-nothing change in both amplitude and duration, a few hundred seconds before seizure-like activity began – a sufficient length of time to provide a helpful warning of an impending seizure. The change in the post-synaptic response then persisted for the remainder of the recording, indicative of a state change from a pre-epileptic to a pro-epileptic network. This occurred in parallel with a large increase in the stimulation-triggered Ca^{2+} entry into pyramidal dendrites, and a step increase in the number of postsynaptic somatic action potentials, both consistent with a reduction in the threshold for dendritic action potentials. In 0 Mg^{2+} bathing media, the reduced threshold was not associated with changes in glutamatergic synaptic function, nor of GABAergic release from either parvalbumin or somatostatin interneurons, but simulations indicate that the step change in the optogenetic response can instead arise from incremental increases in intracellular [Cl^-]. The change in the response to

stimulation was replicated by artificially raising intracellular [Cl^-], using the optogenetic chloride-pump, Halorhodopsin. By contrast, increases in extracellular [K^+] cannot account for the firing patterns in the response to stimulation, although this, and other cellular changes, may contribute to ictal initiation in other circumstances. We describe how these various cellular changes form a synergistic network of positive feedback mechanisms, which may explain the precipitous nature of seizure onset. This model of seizure initiation draws together several major lines of epilepsy research and as well as providing an important proof-of-principle regarding the utility of open-loop brain stimulation for clinical management of the condition.

Author affiliations:

Newcastle University Biosciences Institute, Medical School, Framlington Place, Newcastle upon Tyne, NE2 4HH, UK

[†]Present address: Queen Square Institute of Neurology, University College London, UK

[‡]Present address: Department of Cell Biology and Physiology, Brigham Young University, Provo, UT, USA

Correspondence to: Andrew Trevelyan

Newcastle University Biosciences Institute, Medical School, Framlington Place, Newcastle upon Tyne, NE2 4HH, UK

E-mail: andrew.trevelyan@ncl.ac.uk

Running title: Active probing of ictogenic transition

Keywords: dendritic plateau potentials; voltage-gated Ca^{2+} channels; optogenetics; chloride; potassium

Introduction

Brain state transitions are a fundamental feature of neocortical physiology, and may also play a major role in its functional pathology. Currently, however, we lack a coherent understanding of

how these occur. Transitions tend to be rapid, and while these are readily apparent from changes in brain rhythms[1], the precipitating cause may be invisible to passive recording methods. Identifying such latent influences may lead to improvements in predicting brain state transitions, which would have great practical significance in clinical practice, most notably for epilepsy. While seizures only occur in small numbers of individuals (lifetime incidence is less than 3%), their inherent unpredictability causes great distress, and imposes significant constraints on these individuals' lives.

Recent advances in implantable brain recording and stimulation technology has provided a great wealth of recordings of human seizure activity patterns, but with only limited progress in estimating when seizures are likely to occur[2,3]. There are several difficulties. One issue is whether the key determinants are actually accessible to passive recording methods. A second is that in chronically epileptic brains, if the underlying driving force wanes spontaneously, then the seizure risk might have been assessed (correctly) as being high without a seizure ensuing, making the association less evident: in this case, it may be unclear whether this is because the algorithm worked appropriately, but the seizure risk naturally abated, or if the algorithm failed. In this regard, acute seizure models in transgenic mice offer several advantages for examining biomarkers of seizure initiation (ictogenesis). Ictogenesis develops with a highly characteristic pattern and time course in these models (Figure S1), and once started, the seizure-like ("ictal") activity persists. These acute models thus constitute an ictogenic pacemaker ramp with an identifiable "tipping point", a specific point in time which can be used as a reference for investigating how other network parameters change; for the purposes of this study, we refer to the time prior to the first seizure-like event, as "pre-ictal", and after it as "post-ictal". We use these models to explore the utility of an "active probing" employing cell-specific optogenetic activation. We report two findings of potential significance to clinical practice: that ultra-low frequency stimulation appears to delay the ictogenic process, and that the evoked postsynaptic potential (eEPSP) changes shape shortly before the onset of seizure-like activity. The time-frame of the change, occurring a few hundred seconds prior to the first seizures, is sufficiently long to be clinically useful, either allowing for closed-loop control through an implanted stimulation-recording device[4], or simply to provide an alert to the individual.

Materials and methods

A table of the experimental resources is provided in Supplementary information (Table 1). All animal handling and experimentation were performed according to the guidelines specified by the UK Home Office and Animals (Scientific Procedures) Act 1986, and approved by the Newcastle University Animal Welfare and Ethical Review Body (AWERB #545). Mice were housed on a 12h light/dark cycle, where possible, with littermates, and all mice were provided access to food and water *ad libitum*. All mice used were young adults (6-24 weeks, both male and female, weight range 21-35g) from the C57BL/6 line.

For cell-type selective expression of the relevant gene of interest, channelrhodopsin2 (ChR2), halorhodopsin (HR), or GCaMP6f, mice expressing the floxed gene were crossed with mice expressing Cre-recombinase under neuronal subtype-specific promoters EMX-1 (B6.129S2-Emx1tm1(cre)Krj/ J; Jackson Laboratory stock number 5628), PV (B6;129P2-Pvalb < tm1(cre)Arbr>/J; Jackson Laboratory stock number 8069), or Sst (B6N.Cg.Ssttm2.1 (cre)Zjh/J; Jackson Laboratory stock number 18973).

Slice preparation

Mice were sacrificed by cervical dislocation, the brain removed, and sliced in ice cold cutting solution (in mM): 3 MgCl2; 126 NaCl; 26 NaHCO3; 3.5 KCl; 1.26 NaH2PO4; 10 glucose. Horizontal slices containing both neocortex and hippocampus proper (z = -3.1–4.7mm) were taken using a Leica VT1200 vibratome (Nussloch, Germany) at a thickness of 300µm for patch recordings and 400µm for field recordings. Slices were immediately transferred to a holding chamber and incubated at room temperature for >45 min prior to recording in artificial cerebrospinal fluid (aCSF) containing (in mM): 2 $CaCl_2$; 1 $MgCl_2$; 126 NaCl; 26 $NaHCO_3$; 3.5 KCl; 1.26 NaH_2PO_4; 10 glucose. All solutions were bubbled with carbogen (95% O_2, 5% CO_2) throughout.

In vitro electrophysiology

Local field potentials were recorded in interface recording chambers in which slices were superfused with carbogenated aCSF maintained at a temperature of 34±1°C. The rate of the perfusate circulation was maintained with a peristaltic pump at ~3ml min^{-1} (Watson Marlow). Borosilicate glass microelectrodes (GC120TF-10; Harvard apparatus, Kent) were pulled using an

electrode puller (Model-P87, Sutter Instruments, CA, USA) and filled with aCSF. Recordings were obtained with electrodes at a resistance of 1-3MΩ. Analog signals were acquired using in-house built headstages (10x gain) connected to BMA-931 AC (0.1Hz) differential amplifier (Dataq instruments, Akron, USA) with the gain set appropriately for the recording between 200-500. Amplified signals were digitised at ≥10kHz using a Micro 1401-3 data acquisition unit (Cambridge Electronic Design, UK), bandpass filtered at 1-3000Hz, and stored on a computer using Spike2 (V7.2 or later) acquisition software (Cambridge Electronic Design, UK).

For patch clamp recordings, slices were bathed in carbogenated aCSF perfused at 3-5 ml min^{-1} and heated to 34±1°C. Recordings were made using 4-7MΩ borosilicate glass microelectrodes (GC150F-10, Harvard apparatus, Kent). Electrodes were filled, unless otherwise stated, with K^+ -gluconate-based filling solution containing (in Mm): 125 K-gluconate, 6 NaCl, 10 HEPES, 2.5 Mg-ATP, 0.3 Na_2-GTP. Electrode filling solutions were pH adjusted to 7.3 with KOH and osmolarity adjusted to 280-290mOsm. Patch clamp data were acquired using pClamp software v10.5, Multiclamp 700B, and Digidata acquisition board (Molecular Devices, CA, USA). Signals were digitised with a sampling frequency of 10 kHz.

In vivo electrophysiology

For acute *in vivo* recordings, mice were initially anaesthetised by intraperitoneal injection of urethane (20% w/v in 0.9% sterile saline) at a dose of 0.1ml per gram weight. Anaesthesia was supplemented during craniotomy surgery with 1-2% isoflurane (IsoFlo, Zoetis) in oxygen 1-1.2L $min^{-1.}$ Mice were head fixed in a stereotactic frame. Isoflurane was discontinued once the craniotomy was complete, and at least 20 minutes prior to recording. Internal temperature was monitored by a rectal thermometer and maintained with a thermoregulatory blanket. A dental drill (RAMPower, RAM) was used to make small craniotomies (typically 2-3mm diameter), the dura removed to facilitate penetration with the multielectrode probes, and the cortical surface kept moist with 0.9% saline. Electrophysiological signals were recorded using a 4x4 multielectrode array (NeuroNexus, electrode separation 200µm, recording sites 1250$µm^2$, impedance <3MΩ at 10kHz. Signals were amplified and digitised by a Plexon AC amplifier (MAP Data Acquisition, Hkl3, PLEXON), and were amplified and digitised at 25kHz. Data was stored using Sortclient (V3) software. Optogenetic stimulation was delivered from an adjustable-intensity mountable 470nm LED, through an optic fibre and matched cannula (Ø400µm,

ThorLabs) driven from Spike2 via a Micro 1401-3 data acquisition unit (Cambridge Electronic Design, UK).

Optogenetic manipulations

For ChR2 stimulations, cortical tissue expressing ChR2 under the relevant promoter were stimulated by focal illumination of superficial neocortcex with an optic-fibre coupled LED cube (470nm, Thorlabs). Short stimulations (5ms) were applied at ultra-low frequencies, with an interval of 5, 10, 30, and 60s. Extracellular and/or patch recordings were taken outside the illuminated field.

For halorhodopsin chloride loading experiments, slices were prepared from mice bred to express enhanced Halorhodopsin (eNpHR3.0) in pyramidal cells, under the CamK2a promoter. Extracellular recordings were made from the supragranular layers of cortex, following periods of illumination for several seconds (1-10s) with 561nm yellow light (Thorlabs), to activate the Halorhodopsin pump, a protocol which has been shown by previous work to induce a positive shift in E_{GABA} of up to 20mV (Alfonsa et al. 2015). Each illumination was followed by an electrical stimulation, delivered to superficial neocortex (0.1-4V, 100µs duration) using a Digitimer DS3 electrical stimulator. This stimulation was delivered at a delay of 500ms with respect to the light-off, to allow us to separate the electrographic effects of the optogenetic activation from the evoked field EPSP.

Acute epilepsy models

Epileptic activity was evoked using two acute epilepsy models, the zero-magnesium and 4-AP models. In the zero-magnesium model, brain slices were perfused in conventional aCSF, except with Mg^{2+} ions excluded, containing (in mM): 2 $CaCl_2$, 126 NaCl, 26 $NaHCO_3$, 3.5 KCl, 1.26 NaH_2PO_4, 10 glucose. In all experiments, slices were positioned, and electrodes were placed before the perfusate was switched to $0Mg^{2+}$ aCSF. In the 4-AP model, slices are perfused with aCSF containing the voltage-gated potassium channel blocker, 4-aminopyridine at 100µM, a blocker with high affinity for K_V3 channels, and which generates reproducible interictal-like discharges and sustained seizure-like events.

In *in vivo* experiments, seizures were reliably generated by intracortical injection of 4-AP which evoked a focal seizure that subsequently generalised within 40 minutes. This allowed the

recording of healthy tissue which was subsequently recruited as the seizure spread. 4-AP (500nl, 15mM in 0.9% sterile saline) was injected at a rate of 1µl/min, 500µm deep from the pia using a Hamilton syringe and 35G nanofill needle (Hamilton, UK). Small volume intracortical injection of 4-AP has been reported to have a diffusion limit of 1mm, meaning that tissue recruited at a locus >1mm from the injection site are minimally affected by the pharmacological action of 4-AP, and show physiological response to the adjacent epileptic region of cortex (Wenzel, et al., 2017).

Dendritic calcium imaging

Brain slices were prepared as described and submerged in aCSF and perfused at a rate of 3-4ml min^{-1} and heated to 34±1°C. Local field potentials were recorded with extracellular electrodes described above, and digitised at 10kHz (Digidata 1440, Multiclamp, Axon Instruments), and stored using Thorlabs software (ThorSync, V3.2, and ThorImage, V3.2). Images were captured using a Bergamo II 2-photon microscope (ThorLabs), exciting the sensor with a MaiTai laser (SpectraPhysics) at 940nm through a 16X objective lens (water immersion, NA 0.8, Nikon). Acquisitions were taken at 30Hz in 512x512 resolution, scanning in both directions with a galvo-resonant scan head. 1.5s imaging periods were centred around electrical stimulations (0.1-4V, duration of 100µs, Digitimer DS3) delivered at 0.016Hz (stimulating every 60s), via a θ-glass borosilicate electrode filled with aCSF, for the duration of the experiment.

Computational modelling

A compartmentalised single-cell model was developed using the NEURON simulation environment (Hines & Carnevale, 2001). The 3D morphology of the model was adapted from Louth et al. (2018)[5], for investigating the effects of changing E_{GABA} on the response to synaptic excitation in the apical tuft. As values for channel distribution and conductance in cortical pyramidal cells have previously been empirically measured and published for the NEURON modelling environment, published values were used to constrain this model. Typical values for the biophysical properties of the cell were used, with Ri = 150 Ω cm^{-1}, resting Rm = 60 kΩ cm^{-2}, and Cm = 1 µF cm^{-2} (Migliore, et al., 2003), and were set to be uniform across the cell. I_h (0.0002 mS cm^{-2}) and leak currents were included with reversal potentials set to -30mV and -90mV respectively (Migliore, et al., 2003). Classic Hodgkin-Huxley conductances were included at the soma; KV (type A) channels at conductance of 0.04mS cm^{-2}, NaV channels at 0.0005 mS

cm^{-2}. Excitatory synapses were modelled using an extension of the Exp2Syn class in NEURON. Briefly, the Exp2Syn class is a general class for synapses with a conductance described by a sum of two exponentials with rate constants τ_{rise} and τ_{decay}, here denoted τ_1 and τ_1.

$$G = a \cdot \left(e^{\frac{-t}{\tau_1}} + e^{\frac{-t}{\tau_2}} \right)$$

In excitatory synapses the values for time constants for AMPA (τ_{rise} = 0.2ms; τ_{decay} = 2ms) and NMDA receptors (τ_{rise} = 3ms; τ_{decay} = 35ms) were derived from the empirical measurements made by Shulz et al. The threshold for voltage-dependent unblocking of NMDARs was set at -16mV (Kampa, et al., 2004)[6]. The conductances for both AMPA and NMDA were set to 0. 14 nS, at synapses at a density of 0.5 μm^{-2}. The voltage dependency of the NMDAR current was modelled as in Shulz et al. with the function:

$$gN(v) = gmax\ (1 + 0.2801[Mg^{2+}] \cdot e^{-0.087(v+10)})$$

Where v is in mV and the Mg^{2+} concentration is 1mM.

At inhibitory synapses both rectifying and non-rectifying $GABA_A$ receptors were included, as outward rectifying channels were reported to powerfully constrain dendritic depolarisation (Schulz, et al., 2018). $GABA_A$ synapses were included with a conductance of 0.7 nS, with τ_{rise} = 0.5ms, and τ_{decay} = 15ms (Shulz, et al., 2018). Outward rectifying $GABA_A$ channels were again modelled by expanding the Exp2Syn class (Shulz, et al., 2018), and τ_{rise} to 1ms, and τ_{decay} to 30ms, for membrane voltages above -52mV. Subsets of GABAergic synapses at 0.1 μm^{-2} were activated simultaneously with excitatory synapses. Synapse numbers and distribution were taken from Bloss et al (2016)[7]. Voltage-gated calcium channel (VGCC) conductances were included as described in Lazarewicz et al. (2002), which implements L- and T-type calcium channels according to their distribution in CA1 pyramidal neurons. Here Ca_L and Ca_T conductances have been added. The density of Ca_L conductance is set across the dendritic tree at 0.0013 mS cm^{-2}, and Ca_T in the soma and dendrites within 100µm path distance to the soma at 0.001 mS cm^{-2} (Lazarewicz, et al., 2002)[8]. In order to simulate lateral cortical afferent stimulation, and replicate the experimental protocol, only the apical tuft was stimulated. Excitatory and inhibitory synapses were activated simultaneously to simulate feedforward inhibition which is typically concomitant with excitatory drive *in vivo* [9,10]. Increasing numbers of excitatory synapses in the dendritic tuft were activated for a range of values of E_{GABA} (- 70 to -40mV) to identify the threshold level of

excitation for eliciting a plateau potential. No proximal synapses were added, and no background synaptic noise was included, for simplicity. For clarity of presentation, somatic Na_V channels were silenced to generate the dendritic potentials presented.

Quantification and Statistical analyses

In all cases, data were analysed using custom MATLAB code, and automated where possible.

For analysis of miniature EPSCs (miniEPSCs), a custom written MATLAB script was used to identify the synaptic events using by deconvolving raw traces with a template model EPSC, based on the sum of two exponentials (as described earlier in the "Computational modelling" section). The time constants for model were derived from the best fit to an average of 3-5 manually selected miniEPSCs (Figure 4.5B). Traces were then deconvolved against the fitted model to identify events automatically through the recording. A minimum of 200 EPSCs were analysed per recording.

Data availability

Data will be made available upon request to the authors.

Results

Ultra-low frequency active probing is anti-ictogenic

We took a combined optogenetic, electrophysiological, and imaging approach, using various acute seizure models, to identify key changes in cortical networks that were most closely associated with the initiation of seizure-like activity (SLEs). Specifically, to identify latent changes in the network which are not readily apparent in passive recordings, we developed an optogenetic "active probing" paradigm. We prepared brain slices from mice expressing channelrhodopsin in pyramidal cells, and used light to stimulate this population of cells in isolation. Ictogenesis was induced either by removing Mg^{2+} ions ("0 Mg^{2+}" model) from the artificial CSF (aCSF, Figures 1B, S1), or supplementing it with the convulsant, 4-aminopyridine, 4-AP, (Figure S1). In control recordings, both these models trigger electrographic "seizure-like events" (SLEs) that closely mimic those recorded clinically in humans, and with latencies of

2840 ±1159s (n = 13), and 2068 ±1067s (n=5) respectively. Importantly, prior work has shown that these two models differ in their ictogenic mechanism[11], so any commonalities shared by both models should be considered noteworthy.

Brain stimulation can be used to trigger seizures, so to minimize this risk, we stimulated with a single short (10ms) flash of light (488nm), delivered focally to the superficial layers (centred on layer 1) of neocortex, and at low intensity, such that the fEPSP amplitude was larger than the baseline activity, but substantially lower than the maximum evoked response. On the other hand, brain stimulation may also have anti-epileptic effects, as illustrated by vagal nerve stimulation[12] and intracranial stimulation, both in animal models and in humans[13]. The anti-epileptic effect has typically been achieved by relatively high frequency stimulation, between 1-200Hz[14-18]. Interestingly, we found marked anti-ictogenic effects *in vitro* at far lower stimulation frequencies (0.2 - 0.033Hz; period of stimulation 5-30s; Figure 1). We made direct comparisons of stimulated and non-stimulated (control) brain slices bathed in 0 Mg^{2+} aCSF, prepared from the same animal and recorded simultaneously in the same chamber. When stimulated every 5-30s, there were highly significant reductions in the total number of SLEs recorded in the first hour (0.2Hz, $p < 0.01$, n = 17; 0.1Hz, $p < 0.01$, n = 14; 0.033Hz, $p < 0.05$, n = 7, paired Wilcoxon). There was also a large reduction in the progression to seizure like activity at these stimulation frequencies. To quantify this, we performed a binomial analysis of the probability of the stimulated brain slice seizing prior to the non-stimulated slice, in our paired recordings, which showed highly significant differences at 0.2Hz ($p = 0.02$, n = 17 paired recordings) and 0.033Hz ($p = 0.01$, n = 7 paired recordings) and a marginal difference at 0.1Hz ($p = 0.09$, n = 14 paired recordings). This anti-ictogenic effect was only lost when stimulation frequency was reduced to 1/min (0.017Hz). Since our primary interest was to study the actual transition, we therefore used this lowest frequency of stimulation (0.017Hz) for our subsequent investigations, so that we could record seizure-like activity generally within an hour.

Proactive assays reveal binary switch in network excitability before seizure onset

Pharmacological dissection of the optogenetic fEPSP, done by first applying glutamatergic blockers (APV and NBQX), followed by adding tetrodotoxin to block Na^+ channels, showed that it had components attributable to the channelrhodopsin current, as well as evoked action

potentials and postsynaptic synaptic currents (Figure 2Aii,iii). Critically, the evoked fEPSP was very stable in normal ("baseline") aCSF (Figure S2). The wash-out of Mg^{2+} ions resulted in a small, rapid change in the fEPSP (latency = 495 ± 75s, Figure S3), the latency being only fractionally longer than the dead-space clearance time for the perfusion system (~3-4mins), and similar to the latency for other drug applications (Figure 2B); we attributed this fEPSP change, therefore, to the direct pharmacological effects of the solution change. Critically, the SLE latency was almost an order of magnitude longer than the latency of the direct pharmacological effect (Welch's t-test, $p<0.001$; Figure S3). We concluded from this that SLEs were only indirectly caused by the pharmacological manipulation, and that there must therefore be other, much slower, latent, changes within the network that underlie the network transition.

During this protracted SLE latent period, the fEPSP remained very stable, until there occurred a further sharp increase of almost 2-fold in amplitude (normalised mean = 1.9 ±0.4; Figure 3B,C) and over 5-fold in duration (normalised mean half-width = 5.04 ±2.38; latency = 1900-4050s; Figure 3C). These changes occurred in tandem (Figure 3C), with a sudden step change at a single event. A third metric, the area-under-the-curve (AUC), approximates to the product of the half-width and amplitude, and so also showed a similar step change occurring at the same time (Movie 1). In order to standardize these measures to facilitate comparisons between recordings (Figure 3), we weighted the two variables equivalently, by normalizing both metrics (amplitude and half-width) by the full range of their values, and calculated the centroid value for the first 10 events after the stabilization of the fEPSP immediately following the solution switch. We then derived the Euclidean distances of each event from this centroid point, normalized by the standard deviation of the distance for those first 10 events (the "Euclidean z-score", Figure 3C). In every recording, there was a clear separation of event metrics either side of a single transformative step in the Euclidean distance from the baseline cluster centroid (Figure S4); the average increase in z-score at this step was 56 standard deviations (range of step change in z-score = 14.4 – 154.1; analysis performed on 7 representative recordings (different animals)). Thereafter, in all brain slices examined, the fEPSP remained both larger and longer duration. In most cases, there continued to be some small evolution in the fEPSP, but these changes were small, relative to the single step change, except for instances when the optogenetic stimulus occurred during an SLE, in which case, it triggered a rather small amplitude fEPSP (Figure 3, purple circles).

The stepwise transformation of the fEPSP often happened within a single stimulation period (60s; Figures 2B, 3A, Supplementary Movie 1), and thereafter persisted, indicative of a binary, all-or nothing change. The distribution profile of Euclidean distances from the initial baseline response (first 10 events, once stable after the pharmacological manipulation) typically showed a bimodal distribution, with one very tight cluster of short distances, and a second cluster of much larger values (Figures 3E, S4). The tight cluster always constituted a continuous sequence of the initial evoked responses. In the example shown, the probability of this complete temporal separation of the small (early) and large (late) Euclidean distances occurring by chance was 9.6×10^{-13}; similarly low probabilities were found for all data sets analysed.

Investigations of the precise time course of this transition requires a higher sampling rate than stimulating every 60s. We therefore examined the transitions in the few brain slices stimulated at 10s intervals that did progress to having SLEs (Figures S5 and S6). We examined 4 different metrics: amplitude, half-width, integral and the high-gamma power (80-300Hz). Which of these yielded the clearest step change differed between recordings, but in all 5 brain slices, we identified step changes of over 50% change from baseline to maximal, in at least 2 of the 4 metrics, within 1 or 2 stimuli (10-20s; Figure S6). Notably, the changes in all metrics were aligned with each other, and also to the imminent start of the first SLE.

As such, our optogenetic assay identified a discrete step change that was otherwise latent within the network. Even though this was only revealed by stimulation, it appeared to represent a tipping point within the network, from one state to another. Remarkably, this tipping point occurred consistently, in all brain slices, shortly before the first SLE (Figure 3; mean time between the transition event and the first SLE = 406.8 ±316.3s; range of 1 – 12mins; n = 16; correlation of latencies of fEPSP transformation and first SLE, $r^2 = 0.86$, $p < 0.01$). Importantly, the initial SLEs did not arise directly from a stimulation (Figure 3D), but rather, appeared to arise spontaneously. Once the ictal activity was already firmly established, with many prior SLEs having already occurred, epileptic discharges were at times triggered by the simuli.

A striking feature of the 0 Mg^{2+} model is that hippocampal epileptiform discharges start much later (4879.1 ± 1222.8s; n = 16) than those in neocortex (2840 ± 1159s; p = 0.01; Students' t-test; Figures 2D, S5), even though both brain areas were simultaneously exposed to the same pharmacological manipulation[19]. We therefore examined how the fEPSP transformation occurred

in the two brain areas, alternating stimulation of neocortex and the CA3 Schaffer collateral pathway (Figure S5) to avoid crosstalk or interference between responses. The transformation of fEPSPs at the two sites did not coincide; rather, the hippocampal fEPSP occurred long after both the neocortical transformation and the initial neocortical seizure activity (Figure 3B), but just prior to the onset of the local (hippocampal) seizure activity (Figure 2Ei). In both cases, the fEPSP transformation maintained its close temporal association to the local recruitment to epileptiform activity (hippocampal fEPSP / SLE latency correlation, $r = 0.94$, $p < 0.01$, $n = 16$; Figure 2Eii). We further examined the timing of transformation of the fEPSP in a range of ictogenic preparations with other manipulations (Figure 4): (1) $0Mg^{2+}$ with other pharmacological blockers to alter the rate of epileptiform evolution; (2) in brain slices bathed in 4-AP, and (3) *in vivo*, following a focal injection of 4AP (n=5, Figure 4A); in all cases, a precise, one-to-one relationship was found between the transformed fEPSP and the onset of seizure-like activity (Figure 4B, $r^2 = 0.924$, gradient = 1.0055 ± 0.0403; not significantly different from 1, 2-tailed t-test, $p = 0.5517$). Importantly, in all cases, at both neocortical and hippocampal sites, the fEPSP transformation occurred prior to the start of the local ictal activity (Figures 2D,E and 4B – all points lie above the dotted line; y intercept = 427 ± 151s; 1-tail t-test significantly different from 0, $p < 0.001$). We conclude therefore that active probing of network excitability provides a direct indication of when seizure-like activity will start, in all acute ictogenic models tested.

The transformed fEPSP is associated with an increased dendritic excitability

Interestingly, there was no change in miniature EPSCs amplitude, frequency or kinetics between cells recorded after seizure-like activity was established (Figure S6, n = 6 brain slices), compared to the baseline measurements (n = 7 brain slices), indicating that fEPSP transformation did not arise from a rapid potentiation of glutamatergic transmission. Rather, we hypothesized that the change in the optogenetic response arose from supralinear summation of EPSPs, producing dendritic plateau potentials[20] in populations of neurons. Dendritic plateau potentials are commonly associated with two cellular phenomena that could be used to test this hypothesis: Ca^{2+} entry occurring in extended regions of the dendrites, and bursts of action potential firing at the soma[21]. We therefore imaged Ca^{2+} dynamics in pyramidal apical dendrites in response to stimulation, over the time course of the evolving epileptiform activity (Figure 5, Movies 2-4). Prior to the fEPSP transformation, we found highly localized, low amplitude Ca^{2+} transients

limited to the distal tuft. In contrast, after the transformation, each fEPSP was associated with extensive and sustained Ca^{2+} entry throughout the apical dendrites (Figure 5Bi). Furthermore, the transformation in the fEPSP was coincidental with a large increase in the Ca^{2+} signal in the apical trunk and somata of layer 5 pyramidal cells, in response to the stimulation (Figure 5Bii, n = 4 brain slices). Additionally, the firing patterns of layer 5 pyramidal cells in response to the optogenetic stimulation also changed, consistent with our observations of increased 80-300Hz power in the LFP; using cell-attached patch recordings (Figure 5C), we found that the fEPSP transformation was associated with a large increase in the number of action potentials per burst (Figure 5Civ; n = 9 brain slices, p = 0.0003, paired t-test). Since this activity delivers excitatory drive back into the local network, this constitutes a secondary amplification of the optogenetic response, additional to the dendritic potential. In summary, both Ca^{2+} imaging and recordings of altered action potential activity are consistent with our hypothesis that the preictal transformation of the fEPSP represents the occurrence of dendritic plateau potentials in multiple pyramidal cells, indicative of a population change in dendritic excitability.

Factors underlying change in dendritic excitability

We next asked if the change in dendritic excitability is explained by changes in inhibitory control[22,23]. We recorded postsynaptic inhibitory postsynaptic currents (IPSCs) in layer 5 pyramidal cells, in brain slices bathed in 0 Mg^{2+} aCSF, while delivering intermittent (10s period) optogenetic stimulation either to the local parvalbumin- (PV, Figure 6A), or somatostatin- (Sst, Figure 7B) expressing, interneuronal populations. In both cases, there was a pronounced reduction in the amplitude of optogenetic IPSC associated with pathological discharges, but this only occurred very transiently during bursts of intense pre-ictal interneuronal discharges (Figure 6), and at the precise onset of SLEs (and not before). Importantly, the reduction in amplitude recovered fully (Figures 6) after the ictal event, unlike the fEPSP transformation, which persisted. There are thus two critical differences in the relative timing of the changes in IPSCs and the fEPSP (Figure 6C), and so we concluded that the change in the latter does not arise because of altered PV or Sst interneuron function.

While synaptic IPSCs appear to be relatively stable in the pre-ictal period, inhibitory function may be compromised in another way, by rising chloride levels in the postsynaptic neuron.

Chloride has been demonstrated to rise in neurons around the time of recruitment to the seizure, both *in vitro*[24-28] and *in vivo*[29,30], and the loading continues to progress with subsequent events[26]. Importantly for our observation, chloride levels may rise even prior to the initial seizure-like events, as has been observed both using imaging[26] and also using gramicidin perforated patch recordings of pyramidal cells, in brain slices bathed in $0Mg^{2+}$ [31]. As with the other measures of synaptic function, the time course of the chloride changes does not exactly match the sudden all-or-nothing change in the evoked EPSP, but the fact that there is a progressive creeping rise prior to the onset of seizures suggests that intracellular Cl^- levels may still be a critical factor. To investigate this hypothesis, we asked whether loading chloride into neurons could lead to the all-or-nothing transformation in the fEPSP. To do this, we used the light-activated chloride pump Halorhodopsin to drive chloride into the pyramidal neuron population (Figures 7, S6), as demonstrated previously [32,33]. This reliably induced a large increase in both the amplitude (Figure 8C) and time course of the fEPSP (Figure 7D) evoked by electrical stimulation, thereby demonstrating that chloride-loading is sufficient to explain the fEPSP transformation.

Another well documented ionic change associated with the onset of seizures is an increase in extracellular $[K^+]$ [34-38], which is, in any case, coupled also to the rise in intracellular $[Cl^-]$, through the action of the potassium-chloride co-transporter, KCC2[39,40]. The rises in both extracellular K^+ and intracellular $[Cl^-]$, however, might be expected to be graded [24,29,31,36,41], and while these may occur quite quickly, the time course appears fundamentally different from the all-or-nothing change in the fEPSP. To explore this further, we created an anatomically realistic compartmental model of a pyramidal cell, including two important active conductances, VGCCs and NMDA-receptors (NMDA-Rs) within the apical dendritic tree, in order to map out the relationship between these ionic changes and dendritic excitability. We simulated a transient glutamatergic drive onto the apical tuft, to mimic both the experimental optogenetic stimuli and spontaneous network activation, and varied the intensity of stimulation to map out the threshold for a dendritic plateau potential (Figure 8A). The model also included feedforward inhibition, provided by concomitant activation of a distributed GABAergic synaptic population. We then explored how the threshold for dendritic plateau potentials changed as a function of E_{GABA} or of extracellular $[K^+]$. We found that, for a given level of excitatory drive, there was always a sudden step increase in the amplitude and duration of the synaptic response, as E_{GABA} becomes more positive (Figure 8B,C). The threshold glutamatergic drive to trigger a plateau potential, in this

model, showed an almost linear inverse relation to E_{GABA} (Figure 8D). These simulations illustrate how a smooth change in one parameter (here, $[Cl^-]_{intra}$, although similar results may be had by changing other cellular determinants of excitability) may be yield an all-or-nothing change in the response to a steady level of stimulation.

When shifts in both intracellular Cl^- and extracellular K^+ were incorporated, the simulations indicated an interesting divergence of the effects of these two ionic shifts (Figure 8E). Increasing the extracellular K^+ in isolation (columns of the phase plot, Figure 8E) eventually induced a binary switch into a state of persistent depolarization blockade. The self-terminating bursting behaviour was only seen in the top right part of the plot, representing high levels of intracellular Cl^-, even at relatively physiological levels of extracellular K^+. The transition into this bursting phase space, for sufficient glutamatergic drive, was surpassed by very small increases in intracellular Cl^- (horizontal rows of the phase plot, Figure 8E), indicative of a clear threshold effect; increasing extracellular K^+ facilitated this transition, but did not replicate it.

Discussion

The key result we present is a precise temporal association between an all-or-nothing change in response to a small, focal stimulation of pyramidal cells, and the start of seizure-like activity, in various acute models of ictogenesis (Figures 2D,E and 4B). These acute models provide a continuously increasing seizure risk – an ictogenic ramp – which surpasses some seizure threshold at a certain point, with continual seizure-like activity thereafter; this constitutes a single, clearly defined tipping point which typically, in these models, does not reverse. In contrast, the chronic epileptic state, which is of course the true clinical state in humans, represents a far more complex phenomenon, where the underlying forces driving the network to seize may wax and wane. As such, chronic animal models (and also humans) are expected to give a far less precise correlation between any biomarker of ictogenesis, and seizures actually starting, with many false positives (for instance, see ref[2]), and which may therefore detract from the clarity of the results we have presented here. Acute models, therefore, provide an important milestone towards identifying biomarkers of ictogenesis. Importantly, the 4AP and 0 Mg^{2+} models induce seizures by different mechanisms[11,19], so the identification of a biomarker

common to both gives confidence that it will also be seen with spontaneously occurring seizures in the more complex chronic condition.

Testing in chronic models is, of course, the critical next step in translating these findings towards clinical use. To this end, it is helpful that intermittent stimulation may also protect the networks from seizing (Figure 1). The precise mechanism by which this happens remains obscure, but it is noteworthy that such a protective mechanism is predicted on theoretical grounds, if there exists a homeostatic feedback mechanism[42]. There are clearly multiple such homeostatic mechanisms manifest in cortical networks[43-46], although our data appear to exclude synaptic scaling (Supplementary Figure S8), while gene expression changes might be too slow to account for the effects we present. Another possible mechansims is through activation of group II metabotropic glutamate receptors, which are upregulated following seizures[47], and have a broadly inhibitory action by reducing synaptic release[48].

Investigations into seizure initiation, in recent years, have focused almost entirely upon alterations of interneuronal function[22,49-52], chloride homeostasis[26,31,32,53-56] and extracellular potassium levels[57,58]. In contrast, little attention has been directed towards a possible role of dendritic plateau potentials[20] in the actual ictogenic transition, despite there being a substantial literature associating chronic epileptic phenotypes with changes in expression of various ion channels that influence dendritic excitability, including voltage-gated Ca^{2+} channels[59], I_{Nap} [60], I_A [61], I_h [62,63] and SK-type K^+ channels[64] (see also reviews[65,66]). The importance of dendritic action potentials in ictal pathophysiology is further suggested by an influential model of the paroxysmal depolarizing shift[23,67-69], incorporating voltage-gated Ca^{2+} channels (VGCCs), although this work did not focus upon the actual transition into seizures.

An important, if subtle, point is that the cellular bistability is the product of these active conductances, but that many key underlying factors that affect seizure susceptibility are actually changing gradually. We illustrate this point by modelling $[Cl^-]_{intra}$ and $[K^+]_{extra}$ (Figure 8) but the same point is equally valid for other things that might be changing within a network (density and conductance of inhibitory and excitatory synapses, for example). It is highly significant, therefore, that cellular bi-stability, arising from active conductances such as VGCCs and NMDA receptors, has been proposed to underlie a variety of other network transitions too[70-74].

The simple optogenetic assay identified a tipping point occurring a few hundred seconds

ahead of the onset of seizure-like activity, a time window long enough for an affected person to reach a safe place, or for some anti-epileptic intervention to be delivered. Interestingly, the change is not one of basic synaptic function, but rather, of synaptic integration, with synaptic events summing supra-linearly to produce plateau potentials[20]. Computer simulations indicate that the step change in the firing response to the stimulus may arise even though the underlying parameter changes only incrementally. We illustrate this process by computer simulations and an experimental demonstration of raised $[Cl^-]_{intra}$, but one may also envisage other determinants of cellular excitability (e.g. changes in other dendritic conductances) having a similar effect. Interestingly, raised $[K^+]_{extra}$, on the other hand, results in depolarizing block, and in this particular respect, does not accurately mimic the change in the optogenetic response. Both ionic changes are coupled by the action of the cation-chloride co-transporters, in particular KCC2[39,40], which is significant because raised $[K^+]_{extra}$ will tend to coordinate raised $[Cl^-]_{intra}$ across local populations of neurons. Notably, these ionic changes arise from neuronal activity, and facilitate further activation, and so constitute positive feedback mechanisms, as do dendritic action potentials and the subsequent burst firing of pyramidal cells which feeds more glutamate back into the system. Collectively, these constitute a synergistic network of positive feedback effects[75], which accelerates sharply at a certain point, overcoming various protective negative feedback effects that are embedded within the network[76]. Various high-level mathematical models have been developed, describing seizure initiation in terms of saddle-nodes[77], and network resilience[78] or fragility[79], without specifying the molecular or cellular parameters. Our optogenetics assay now provides a cellular explanation of this critical tipping point, with important implications for future clinical management of the epileptic condition.

Acknowledgments

We would like to thank all members of the Trevelyan laboratory for discussion and help throughout the project. We also thank the support staff in the animal facility at Newcastle University. We also thank Dr Sasha Gartside for help establishing the *in vivo* recordings, Dr Frances Hutchings, for help with the NEURON simulations, and Dr Yujiang Wang, Ed Merricks, Chris Papasavvas, and Professors Gian Michele Ratto, Andrew Jackson and Mike Hausser for comments on the manuscript.

Funding

This work was supported by a Newcastle University PhD studentship (RG), and grants from MRC (MR/R005427/1), Epilepsy Research UK, Wellcome Trust (102037) and EPSRC (A000026).

Competing interests

We declare no competing interests.

Supplementary material

Supplementary material is available at *Brain* online.

References

1. Buzsáki, G. *Rhythms of the brain*, (Oxford University Press, Oxford, 2006).
2. Karoly, P.J., *et al.* Interictal spikes and epileptic seizures: their relationship and underlying rhythmicity. *Brain* **139**, 1066-1078 (2016).
3. Karoly, P.J., *et al.* The circadian profile of epilepsy improves seizure forecasting. *Brain* **140**, 2169-2182 (2017).
4. Zaaimi, B., *et al.* Closed-loop optogenetic control of normal and pathological network dynamics. *Nature Biomedical Engineering* **In the press (pre-print doi 10.21203/rs.3.rs-78230/v1)**(2021).
5. Louth, E.L., Luctkar, H.D., Heney, K.A. & Bailey, C.D.C. Developmental ethanol exposure alters the morphology of mouse prefrontal neurons in a layer-specific manner. *Brain Res* **1678**, 94-105 (2018).
6. Kampa, B.M., Clements, J., Jonas, P. & Stuart, G.J. Kinetics of Mg2+ unblock of NMDA receptors: implications for spike-timing dependent synaptic plasticity. *J Physiol* **556**, 337-345 (2004).

7. Bloss, E.B., *et al.* Structured Dendritic Inhibition Supports Branch-Selective Integration in CA1 Pyramidal Cells. *Neuron* **89**, 1016-1030 (2016).

8. Lazarewicz, M.T., Migliore, M. & Ascoli, G.A. A new bursting model of CA3 pyramidal cell physiology suggests multiple locations for spike initiation. *Biosystems* **67**, 129-137 (2002).

9. Buzsaki, G., Kaila, K. & Raichle, M. Inhibition and brain work. *Neuron* **56**, 771-783 (2007).

10. Doron, M., Chindemi, G., Muller, E., Markram, H. & Segev, I. Timed Synaptic Inhibition Shapes NMDA Spikes, Influencing Local Dendritic Processing and Global I/O Properties of Cortical Neurons. *Cell Rep* **21**, 1550-1561 (2017).

11. Codadu, N.K., *et al.* Divergent paths to seizure-like events. *Physiological reports* **7**, e14226 (2019).

12. Binnie, C.D. Vagus nerve stimulation for epilepsy: a review. *Seizure* **9**, 161-169 (2000).

13. Bergey, G.K., *et al.* Long-term treatment with responsive brain stimulation in adults with refractory partial seizures. *Neurology* **84**, 810-817 (2015).

14. Toprani, S. & Durand, D.M. Long-lasting hyperpolarization underlies seizure reduction by low frequency deep brain electrical stimulation. *J Physiol* **591**, 5765-5790 (2013).

15. Ladas, T.P., Chiang, C.C., Gonzalez-Reyes, L.E., Nowak, T. & Durand, D.M. Seizure reduction through interneuron-mediated entrainment using low frequency optical stimulation. *Exp Neurol* **269**, 120-132 (2015).

16. Shiri, Z., *et al.* Optogenetic Low-Frequency Stimulation of Specific Neuronal Populations Abates Ictogenesis. *J Neurosci* **37**, 2999-3008 (2017).

17. Rashid, S., Pho, G., Czigler, M., Werz, M.A. & Durand, D.M. Low frequency stimulation of ventral hippocampal commissures reduces seizures in a rat model of chronic temporal lobe epilepsy. *Epilepsia* **53**, 147-156 (2012).

18. Levesque, M., *et al.* Paradoxical effects of optogenetic stimulation in mesial temporal lobe epilepsy. *Ann Neurol* **86**, 714-728 (2019).

19. Codadu, N.K., Parrish, R.R. & Trevelyan, A.J. Region-specific differences and areal

interactions underlying transitions in epileptiform activity. *J Physiol* **597**, 2079-2096 (2019).

20. Schiller, J., Major, G., Koester, H.J. & Schiller, Y. NMDA spikes in basal dendrites of cortical pyramidal neurons. *Nature* **404**, 285-289 (2000).

21. Larkum, M.E., Zhu, J.J. & Sakmann, B. A new cellular mechanism for coupling inputs arriving at different cortical layers. *Nature* **398**, 338-341 (1999).

22. Parrish, R.R., Codadu, N.K., Mackenzie-Gray Scott, C. & Trevelyan, A.J. Feedforward inhibition ahead of ictal wavefronts is provided by both parvalbumin- and somatostatin-expressing interneurons. *J Physiol* **597**, 2297-2314 (2019).

23. Wong, R.K. & Prince, D.A. Dendritic mechanisms underlying penicillin-induced epileptiform activity. *Science* **204**, 1228-1231 (1979).

24. Ellender, T.J., Raimondo, J.V., Irkle, A., Lamsa, K.P. & Akerman, C.J. Excitatory effects of parvalbumin-expressing interneurons maintain hippocampal epileptiform activity via synchronous afterdischarges. *J Neurosci* **34**, 15208-15222 (2014).

25. Lillis, K.P., Kramer, M.A., Mertz, J., Staley, K.J. & White, J.A. Pyramidal cells accumulate chloride at seizure onset. *Neurobiol Dis* **47**, 358-366 (2012).

26. Dzhala, V.I., *et al.* Progressive NKCC1-dependent neuronal chloride accumulation during neonatal seizures. *J Neurosci* **30**, 11745-11761 (2010).

27. Isomura, Y., *et al.* Synaptically activated Cl- accumulation responsible for depolarizing GABAergic responses in mature hippocampal neurons. *J Neurophysiol* **90**, 2752-2756 (2003).

28. Fujiwara-Tsukamoto, Y., Isomura, Y., Nambu, A. & Takada, M. Excitatory gaba input directly drives seizure-like rhythmic synchronization in mature hippocampal CA1 pyramidal cells. *Neuroscience* **119**, 265-275 (2003).

29. Sulis Sato, S., *et al.* Simultaneous two-photon imaging of intracellular chloride concentration and pH in mouse pyramidal neurons in vivo. *Proc Natl Acad Sci U S A* **114**, E8770-E8779 (2017).

30. Timofeev, I., Grenier, F. & Steriade, M. The role of chloride-dependent inhibition and the

activity of fast-spiking neurons during cortical spike-wave electrographic seizures. *Neuroscience* **114**, 1115-1132 (2002).

31. Burman, R.J., *et al.* Excitatory GABAergic signalling is associated with benzodiazepine resistance in status epilepticus. *Brain* **142**, 3482-3501 (2019).

32. Alfonsa, H., *et al.* The contribution of raised intraneuronal chloride to epileptic network activity. *J Neurosci* **35**, 7715-7726 (2015).

33. Raimondo, J.V., Kay, L., Ellender, T.J. & Akerman, C.J. Optogenetic silencing strategies differ in their effects on inhibitory synaptic transmission. *Nat Neurosci* **15**, 1102-1104 (2012).

34. Heinemann, U., Lux, H.D. & Gutnick, M.J. Extracellular free calcium and potassium during paroxsmal activity in the cerebral cortex of the cat. *Exp Brain Res* **27**, 237-243 (1977).

35. de Curtis, M., Uva, L., Gnatkovsky, V. & Librizzi, L. Potassium dynamics and seizures: Why is potassium ictogenic? *Epilepsy Res* **143**, 50-59 (2018).

36. Gnatkovsky, V., Librizzi, L., Trombin, F. & de Curtis, M. Fast activity at seizure onset is mediated by inhibitory circuits in the entorhinal cortex in vitro. *Ann Neurol* **64**, 674-686 (2008).

37. Fertziger, A.P. & Ranck, J.B., Jr. Potassium accumulation in interstitial space during epileptiform seizures. *Exp Neurol* **26**, 571-585 (1970).

38. Prince, D.A., Lux, H.D. & Neher, E. Measurement of extracellular potassium activity in cat cortex. *Brain Res* **50**, 489-495 (1973).

39. Rivera, C., *et al.* The K+/Cl- co-transporter KCC2 renders GABA hyperpolarizing during neuronal maturation. *Nature* **397**, 251-255 (1999).

40. Viitanen, T., Ruusuvuori, E., Kaila, K. & Voipio, J. The K+-Cl cotransporter KCC2 promotes GABAergic excitation in the mature rat hippocampus. *J Physiol* **588**, 1527-1540 (2010).

41. Raimondo, J.V., Burman, R.J., Katz, A.A. & Akerman, C.J. Ion dynamics during seizures. *Frontiers in cellular neuroscience* **9**, 419 (2015).

42. Perez-Cervera, A. & Hlinka, J. Perturbations both trigger and delay seizures due to generic properties of slow-fast relaxation oscillators. *PLoS Comput Biol* **17**, e1008521 (2021).

43. Mulroe, F., *et al.* Targeting firing rate neuronal homeostasis can prevent seizures. *Disease models & mechanisms* (2022).

44. Parrish, R.R., Codadu, N.K., Racca, C. & Trevelyan, A.J. Pyramidal cell activity levels affect the polarity of gene transciption changes in interneurons. *J Neurophysiol* **120**, 2358–2367 (2018).

45. Davis, G.W. Homeostatic signaling and the stabilization of neural function. *Neuron* **80**, 718-728 (2013).

46. Turrigiano, G.G., Leslie, K.R., Desai, N.S., Rutherford, L.C. & Nelson, S.B. Activity-dependent scaling of quantal amplitude in neocortical neurons. *Nature* **391**, 892-896 (1998).

47. Doherty, J. & Dingledine, R. Reduced excitatory drive onto interneurons in the dentate gyrus after status epilepticus. *J Neurosci* **21**, 2048-2057 (2001).

48. Bocchio, M., *et al.* Group II Metabotropic Glutamate Receptors Mediate Presynaptic Inhibition of Excitatory Transmission in Pyramidal Neurons of the Human Cerebral Cortex. *Frontiers in cellular neuroscience* **12**, 508 (2018).

49. Trevelyan, A.J. & Schevon, C.A. How inhibition influences seizure propagation. *Neuropharmacology* **69**, 45-54 (2013).

50. Chang, M., *et al.* Brief activation of GABAergic interneurons initiates the transition to ictal events through post-inhibitory rebound excitation. *Neurobiol Dis* **109**, 102-116 (2018).

51. Avoli, M., *et al.* Specific imbalance of excitatory/inhibitory signaling establishes seizure onset pattern in temporal lobe epilepsy. *J Neurophysiol* **115**, 3229-3237 (2016).

52. Khoshkhoo, S., Vogt, D. & Sohal, V.S. Dynamic, Cell-Type-Specific Roles for GABAergic Interneurons in a Mouse Model of Optogenetically Inducible Seizures. *Neuron* **93**, 291-298 (2017).

53. Pallud, J., *et al.* Cortical GABAergic excitation contributes to epileptic activities around human glioma. *Science translational medicine* **6**, 244ra289 (2014).

54. Alfonsa, H., Lakey, J.H., Lightowlers, R.N. & Trevelyan, A.J. Cl-out is a novel cooperative optogenetic tool for extruding chloride from neurons. *Nature communications* **7**, 13495 (2016).

55. Pavlov, I., Kaila, K., Kullmann, D.M. & Miles, R. Cortical inhibition, pH and cell excitability in epilepsy: what are optimal targets for antiepileptic interventions? *J Physiol* **591**, 765-774 (2013).

56. Cossart, R., Bernard, C. & Ben-Ari, Y. Multiple facets of GABAergic neurons and synapses: multiple fates of GABA signalling in epilepsies. *Trends Neurosci* **28**, 108-115 (2005).

57. Somjen, G.G. & Giacchino, J.L. Potassium and calcium concentrations in interstitial fluid of hippocampal formation during paroxysmal responses. *J Neurophysiol* **53**, 1098-1108 (1985).

58. Somjen, G.G. *Ions in the brain: Normal function, seizures and stroke*, (Oxford University Press, Oxford, 2004).

59. Su, H., *et al.* Upregulation of a T-type Ca2+ channel causes a long-lasting modification of neuronal firing mode after status epilepticus. *J Neurosci* **22**, 3645-3655 (2002).

60. Kearney, J.A., *et al.* A gain-of-function mutation in the sodium channel gene Scn2a results in seizures and behavioral abnormalities. *Neuroscience* **102**, 307-317 (2001).

61. Bernard, C., *et al.* Acquired dendritic channelopathy in temporal lobe epilepsy. *Science* **305**, 532-535 (2004).

62. McClelland, S., *et al.* Neuron-restrictive silencer factor-mediated hyperpolarization-activated cyclic nucleotide gated channelopathy in experimental temporal lobe epilepsy. *Ann Neurol* **70**, 454-464 (2011).

63. Santoro, B. & Shah, M.M. Hyperpolarization-Activated Cyclic Nucleotide-Gated Channels as Drug Targets for Neurological Disorders. *Annu Rev Pharmacol Toxicol* **60**, 109-131 (2020).

64. Cai, X., *et al.* Hyperexcitability of distal dendrites in hippocampal pyramidal cells after chronic partial deafferentation. *J Neurosci* **27**, 59-68 (2007).

65. Poolos, N.P. & Johnston, D. Dendritic ion channelopathy in acquired epilepsy. *Epilepsia* **53 Suppl 9**, 32-40 (2012).

66. Tang, C.-M. & Thompson, S.M. Perturbations of dendritic excitability in epilepsy. in *Jasper's Basic Mechanisms of the Epilepsies* (eds. Noebels, J., Avoli, M., Rogawski, M.A., Olsen, R.W. & Delgado-Escueta, A.) 733-749 (National Center for Biotechnology Information, Bethesda, 2012).

67. Johnston, D. & Brown, T.H. Giant synaptic potential hypothesis for epileptiform activity. *Science* **211**, 294-297 (1981).

68. Traub, R.D. & Miles, R. *Neuronal networks of the hippocampus*, (Cambridge University Press, Cambridge, UK, 1991).

69. Traub, R.D., Miles, R. & Wong, R.K. Model of the origin of rhythmic population oscillations in the hippocampal slice. *Science* **243**, 1319-1325 (1989).

70. Goldman, M.S., Levine, J.H., Major, G., Tank, D.W. & Seung, H.S. Robust persistent neural activity in a model integrator with multiple hysteretic dendrites per neuron. *Cereb Cortex* **13**, 1185-1195 (2003).

71. Major, G., Larkum, M.E. & Schiller, J. Active properties of neocortical pyramidal neuron dendrites. *Annu Rev Neurosci* **36**, 1-24 (2013).

72. Loewenstein, Y., *et al.* Bistability of cerebellar Purkinje cells modulated by sensory stimulation. *Nat Neurosci* **8**, 202-211 (2005).

73. Takahashi, N., Oertner, T.G., Hegemann, P. & Larkum, M.E. Active cortical dendrites modulate perception. *Science* **354**, 1587-1590 (2016).

74. Marder, E., Abbott, L.F., Turrigiano, G.G., Liu, Z. & Golowasch, J. Memory from the dynamics of intrinsic membrane currents. *Proc Natl Acad Sci U S A* **93**, 13481-13486 (1996).

75. Trevelyan, A.J., Graham, R.T., Parrish, R.R. & Codadu, N.K. Synergistic positive feedback mechanisms underlying seizure initiation. *Epilepsy Currents* (2022).

76. Trevelyan, A.J. Do Cortical Circuits Need Protecting from Themselves? *Trends Neurosci* **39**, 502-511 (2016).

77. Jirsa, V.K., Stacey, W.C., Quilichini, P.P., Ivanov, A.I. & Bernard, C. On the nature of seizure dynamics. *Brain* **137**, 2210-2230 (2014).

78. Chang, W.C., *et al.* Loss of neuronal network resilience precedes seizures and determines the ictogenic nature of interictal synaptic perturbations. *Nat Neurosci* **21**, 1742-1752 (2018).

79. Li, A., *et al.* Neural fragility as an EEG marker of the seizure onset zone. *Nat Neurosci* **24**, 1465-1474 (2021).

Figure legends

Figure 1 Ultra-low frequency optogenetic stimulation is anti-ictogenic. (A) Schematic of the recording and optogenetic stimulation arrangement for the brain slice experiments. Focal illumination was targeted to activate presynaptic fibres, with the electrodes at a displaced location to record the postsynaptic response. (B) Summary histogram of the proportion of brain slices showing progression to SLEs within the first hour. (C) Data sets from paired recordings – one unstimulated, "control" brain slice and one stimulated brain slice, exposed to the same ictogenic 0 Mg^{2+} solution, in the same recording chamber – showing the number of seizure-like events (SLEs) recorded in the hour after the solution change. Data is shown for 4 different stimulation frequencies, with periods of 5s, 10s, 30s and 60s. (D) The latency to the first SLE in all brain slices. For both metrics, stimulation at 0.2-0.033Hz significantly delays ictogenesis, and reduces the total seizure load, but this effect is lost at stimulation frequency of 1/60s (0.017Hz).

Figure 2 All-or-nothing transformation of response to optogenetic activation of pyramidal cells occurs shortly before seizure onset. (A1) Schematic showing the *in vitro* recording arrangement in horizontal brain slices prepared from young adult mice expressing channelrhodopsin in pyramidal cells. (Aii) Aligned responses to the optogenetic stimulation at different stages of one example experiment, showing the initial baseline responses (grey, individual traces; light blue, averaged response), the post-transformation response, occurring at

the time of the first SLE (dark blue), and after the subsequent applications of NBQX(40µM) and AP5 (50µM), to block AMPA and NMDA-receptors respectively (green), and finally of TTX(1µM, red trace), to block action potential firing. Note the large residual component that is directly attributable to the channelrhodopsin current. (Aiii) The mean power of these different fEPSP responses (same colour coding). The post-transformation events have a far larger low frequency component, and the inset is the same data plotted with a different y-scale, to show the small differences between the other 3 responses. (Bi) Illustrative LFP recording of neocortical activity. The overlying bar indicates the time of the solution change (filled bar, baseline aCSF; open bar, wash-out of Mg^{2+}). 500ms epochs around each stimulus are coloured blue, to distinguish the spontaneous activity (black) from the evoked activity (blue). (Bii) The change in amplitude and half-width, relative to baseline events. The inset shows higher resolution views of consecutive evoked responses around the time of the fEPSP transformation, and which occurs just before the first seizure-like event. (C) Plots of the amplitude, half-width and area-under-the-curve, for sequential fEPSPs. Also shown is the normalized Euclidean distance from the mean event for the first 10 fEPSPs recorded after the solution switch. (D,E) Examples of the transitions shown in the neocortical (Di, green) and CA1 (Dii, purple) evoked responses (baseline events subtracted). Ei. The difference in latency to first SLA in both areas. Eii. The latency from the transformation of the evoked EPSP to the first SLE ($p < 0.01$, Welch's t-test).

Figure 3 Phase-space plots show a clear, and easily made distinction between the pre-ictal and post-ictal fEPSP metrics. (A) Plot of the fEPSP amplitude and half-width of all the fEPSPs, for the recording shown in Figure 2B. The yellow point indicates the mean event metrics for the first 10 events recorded after the solution switch had stabilized. The black points are those fEPSPs prior to the transformation – note how tight this cluster is. fEPSPs that occur during SLEs are plotted as blue circles. (Bi) An enlarged view of the pre-ictal cluster, as well as the first 6 events after the transformation, joined by a dotted line. Note the 5th event after the transformation, which occurred during the second SLE (trace shown in Bii), and was greatly curtailed. (C) The same data set with the amplitudes and half-widths plotted on a scale normalized to the complete range, to allow the Euclidean distances to be plotted (normalization is necessary in order to weight evenly the two metrics, which have rather different scales otherwise). (D) The effect of an on-going SLE on the fEPSP. (E) The distribution of Euclidean

distances. Note the separation of the pre- and post-transition events by a distance equivalent to 20 standard-deviations (when those events occurring during SLEs (purple) are discounted).

Figure 4 *In vivo* demonstration of transformation of EPSP associated with seizure initiation. (Ai) Schematic showing the *in vivo* recording arrangement and the stepwise change in the evoked response. (Aii) Example local field potential recording of an anaesthetized mouse, which received injection of 4-aminopyridine into occipital cerebral cortex (primary visual cortex). The start of the first seizure is shown at higher resolution in the inset (bottom right). The evoked events are coloured blue, to distinguish these from the spontaneous activity (black). (Aiii) The mean (shadow: standard deviation) trace during the pre-injection baseline period (red), the post-injection period prior to the first seizure (black) and after the first seizure (green). (Aiv) Raster representation of successive optogenetically evoked fEPSPs throughout the recording. Note the transformation immediately before the onset of the first seizure. (Av) Plot of the amplitude of the evoked events versus their durations, colour-coded in the same way. Note the clear separation of the pre- and post-ictal data points, with a single exception (arrowed) which is the very final evoked event prior to the first seizure. (B) Summary plot of all experiments (in vitro and in vivo), showing the close correlation between the time of the fEPSP transformation (abscissa) and the time of the first seizure (ordinate). The red line is the linear fit to the data (gradient = 1.0055 ± 0.0403; no significant difference from the line of equality (black), gradient = 1; p = 0.5517).

Figure 5 The fEPSP transformation reflects the occurrence of dendritic spiking. (A) Schematic showing the *in vitro* recording arrangement in horizontal brain slices prepared from young adult mice expressing GCaMP6f in pyramidal cells. Epileptiform activity was induced by washing out Mg^{2+} ions. The inset shows the apical dendrite trunk of a layer 5 pyramidal cell (scale bar 10µm) (Bi) The change in Ca^{2+} signal in the apical dendrite trunk, recorded for sequential stimuli, and the LFP, recorded from a close extracellular electrode. Synchronous events are colour-coded, with green events prior to the transformation, and red events after. (Bii) Plot showing the parallel changes in half-width of both the dendritic GCaMP6f signal (green) and the LFP, for sequential stimuli. (Ci) Schematic showing the recording arrangement for the

cell-attached recordings from layer 5 pyramidal cells, and the LFP in the supragranular layers (Cii). (Ciii) Example of the binary change in the spiking pattern of the pyramidal cell, just prior to the first seizure, and (Civ) pooled data showing the large increase in firing in all recorded neurons (n = 9 brain slices, 4 mice; *, $p < 0.01$, paired t-test).

Figure 6 Analysis of inhibitory function, relative to the timing of fEPSP transformation. (A) Example recording from a pyramidal cell, held in voltage clamp mode at -30mV, and bathed in 0 Mg^{2+}, resulting eventually in an SLE (the prominent downward deflection in the trace). Throughout the experiment, local PV interneurons were stimulated optogenetically, to induce a postsynaptic IPSC in the recorded pyramidal cell. (B) Equivalent recording, while optogenetically stimulating Sst interneurons. (C) Pooled data (PV, n = 3; Sst, n = 7; recordings were excluded if they showed instability within the period 500s prior to and 100s after the onset of the first SLE), aligned by the time of the first SLE. The different recordings were normalized to the mean over the entire pre-ictal period. The shaded area represents the standard deviation. Note the deviation below baseline (normalized response = 1) only occurs after the seizure onset, and for both data sets is significantly different from unity at a single time point, 20s after the seizure onset (stimulation frequency = 0.1Hz). (Ciii) A histogram of the timing of the fEPSP transformation, for all experiments shown in Figures 1 and 2. Note that the fEPSP transformation invariably occurs ahead of the first SLE, but the change in the input of both interneurons to pyramidal cells only occurs at the onset of the SLE, and recovers at its end.

Figure 7 Chloride loading of pyramidal cells mimics the transformation of fEPSP associated with seizure initiation. (A) Schematic showing the experimental recording arrangement for the chloride-loading into pyramidal cells, induced by prior activation of the optogenetic chloride-pump, Halorhodopsin, with subsequent electrical stimulation of glutamatergic afferents. The stimulating electrode was ~500µm away from the recorded neuron. (B) Example traces, showing the effect of progressively long epochs of Halorhodopsin activation prior to the electrical stimulus. (C) Histograms of the pooled data, showing the effects of chloride-loading on the amplitude and (D) half-width of the evoked fEPSP.

Figure 8 Exploration of the effects of incremental changes of E_{GABA} and E_K, using computational simulations. (A) Structure of the model pyramidal cell, with the locations of the excitatory (green spots) and inhibitory feedforward synapses on the apical tuft. (B) Membrane potential recorded at two sites, in the apical dendrites (top) or at the soma (bottom), showing repeat simulations performed with a constant level of synaptic drive, but with different simulated E_{GABA}, colour-coded as shown in (C), which depicts the increasing amplitude and half-width of the plateau potential, and the number of action potentials for each event. Note the step increase for each parameter, as E_{GABA} becomes more positive. (D) Simulations show that the number of glutamatergic synapses required to trigger a dendritic plateau potential is inversely related to E_{GABA}. (E) A phase plot of the number of action potentials evoked by a single stimulation, in the model, with respect to changes in the reversal potentials of potassium (E_K) and chloride (E_{Cl}). Note the dotted red line; for values of E_K below this line, the events are self-limiting, but above this line, the simulation invariably enters a depolarizing block. Note also, therefore, that binary effect (bottom right) is primarily the consequence of increasing intracellular Cl^-, albeit facilitated by increasing extracellular K^+.

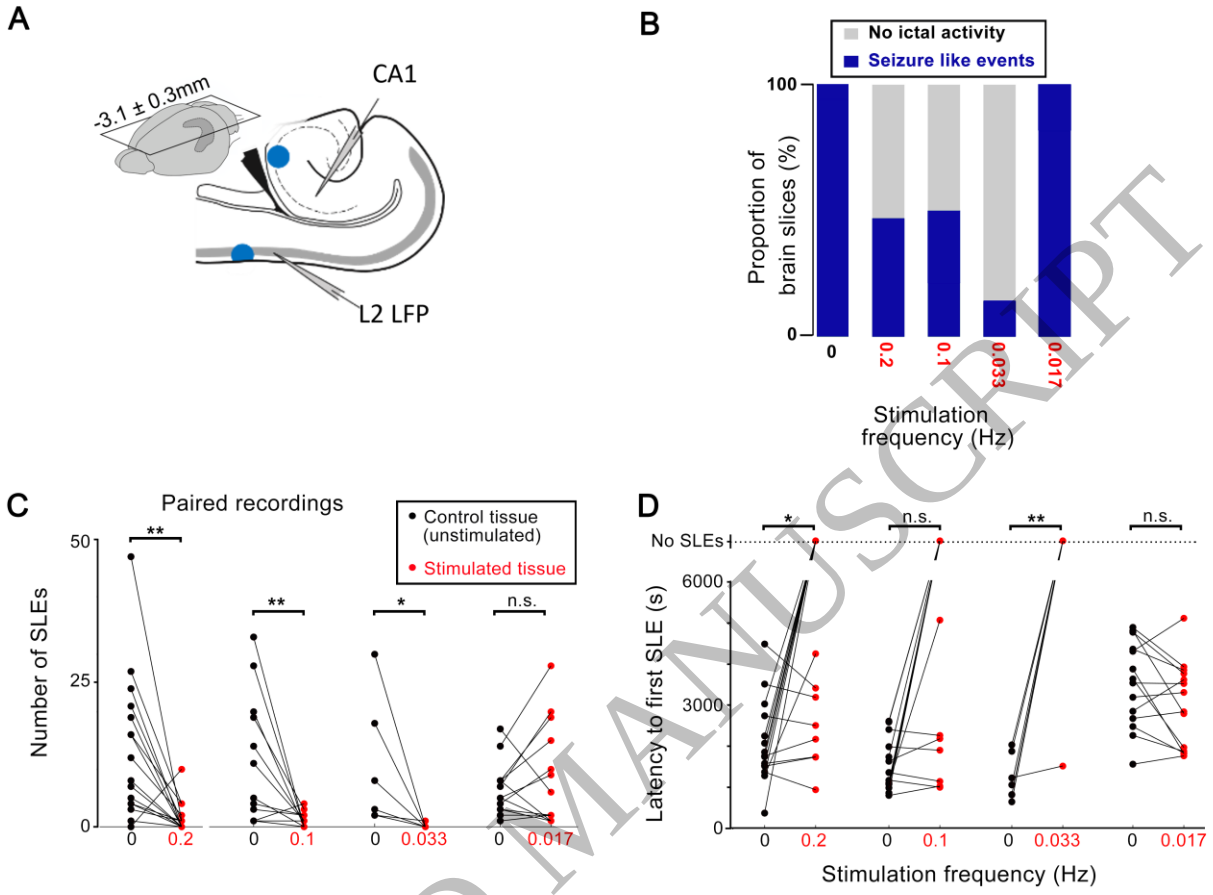

Figure 1
165x120 mm (5.4 x DPI)

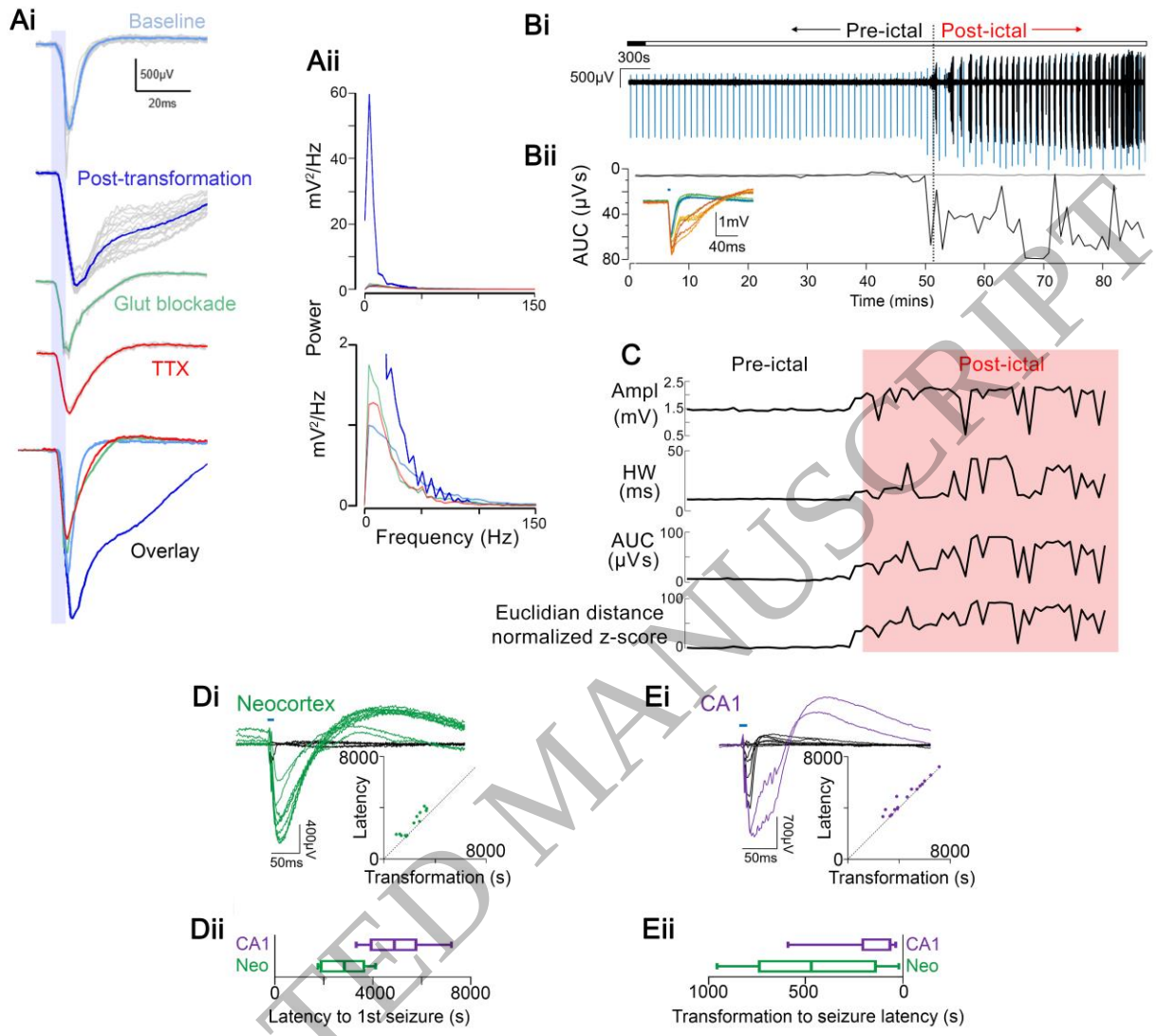

Figure 2
165x151 mm (5.4 x DPI)

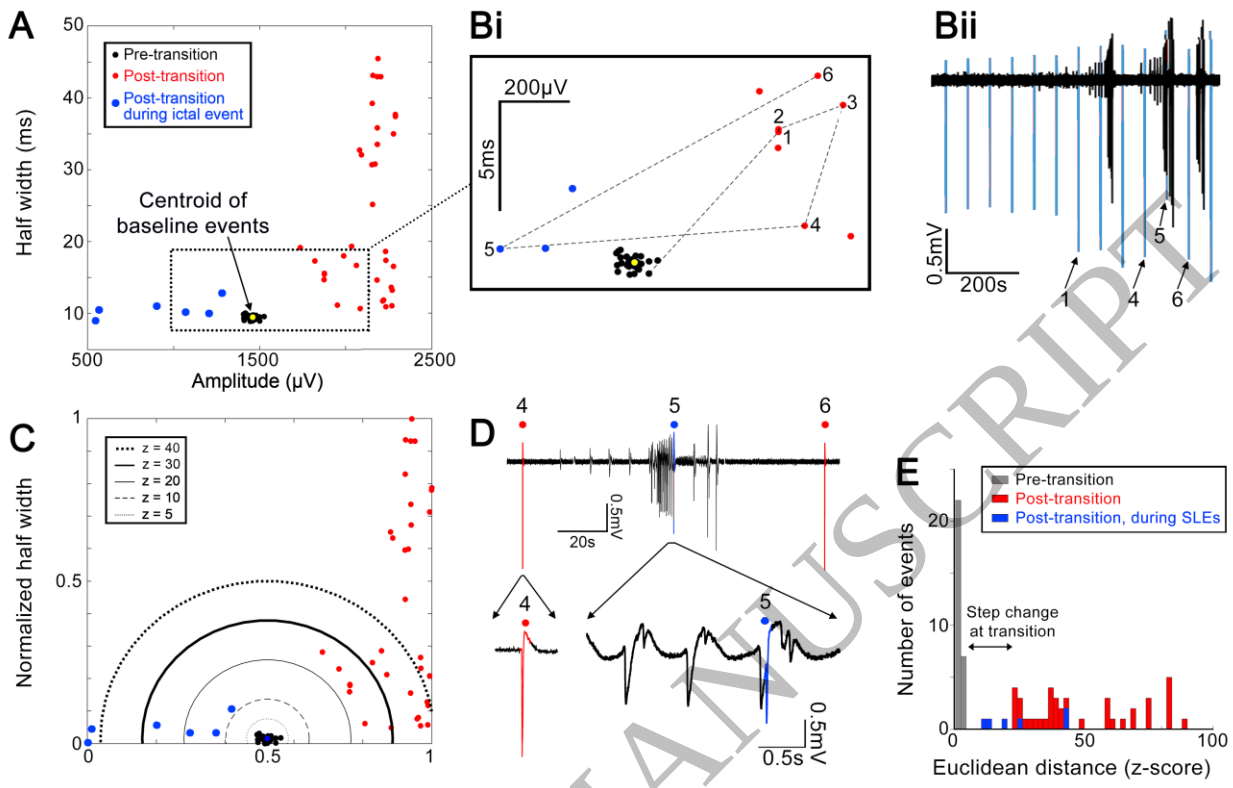

Figure 3
165x104 mm (5.4 x DPI)

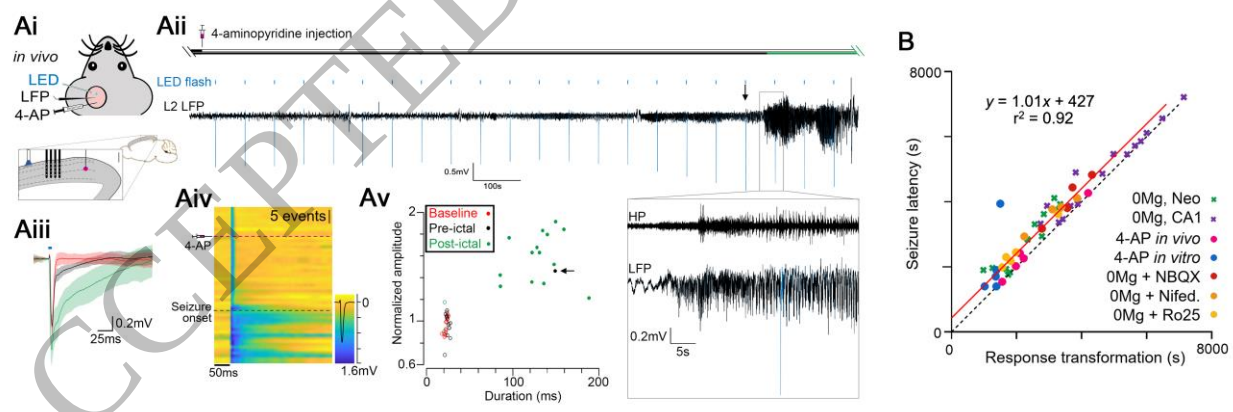

Figure 4
165x56 mm (5.4 x DPI)

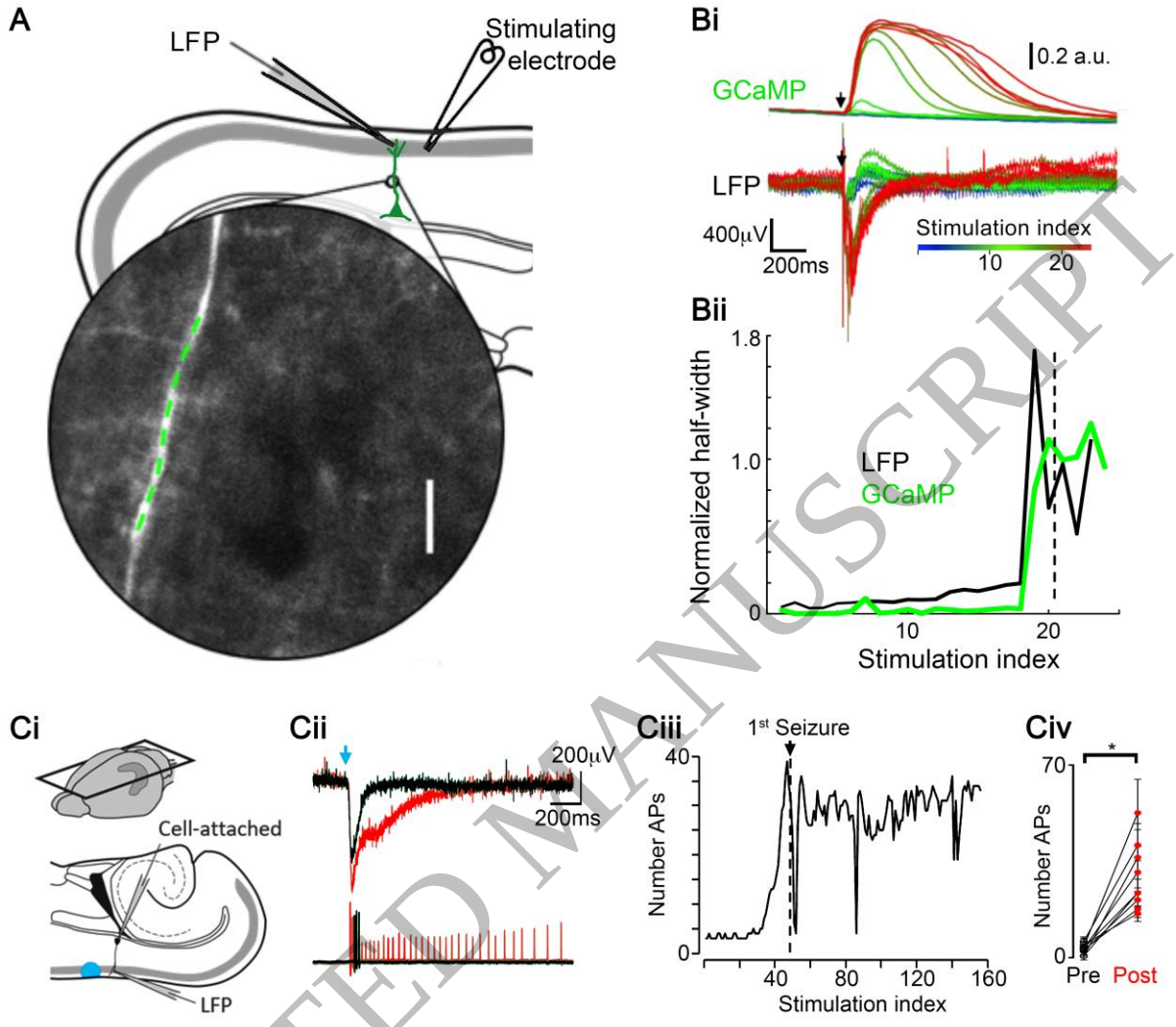

Figure 5
165x144 mm (5.4 x DPI)

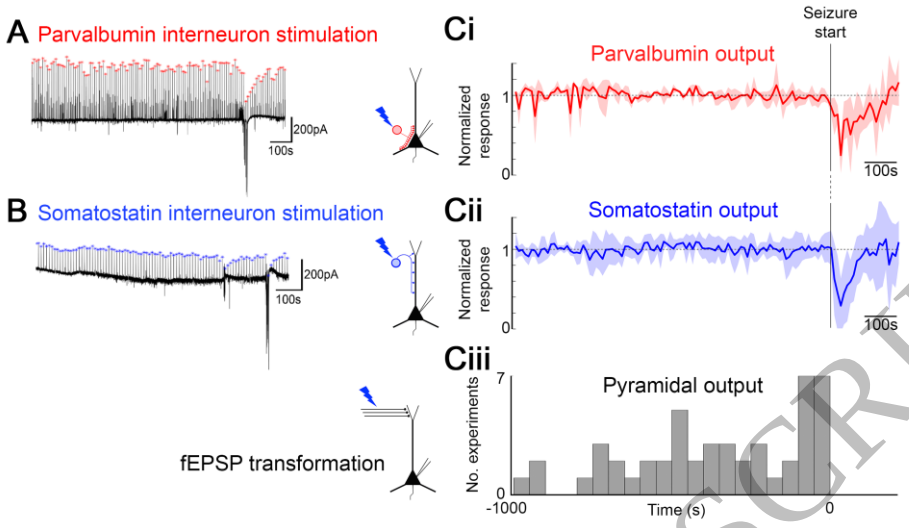

Figure 6
123x70 mm (5.4 x DPI)

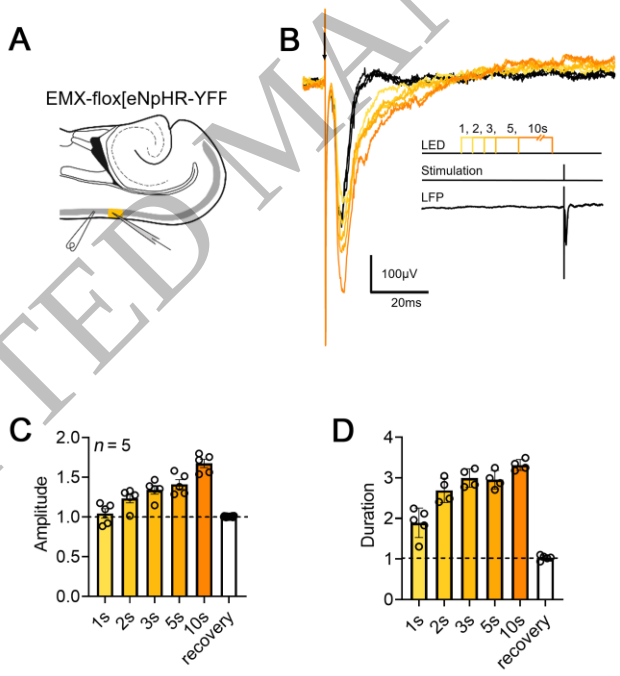

Figure 7
83x90 mm (5.4 x DPI)

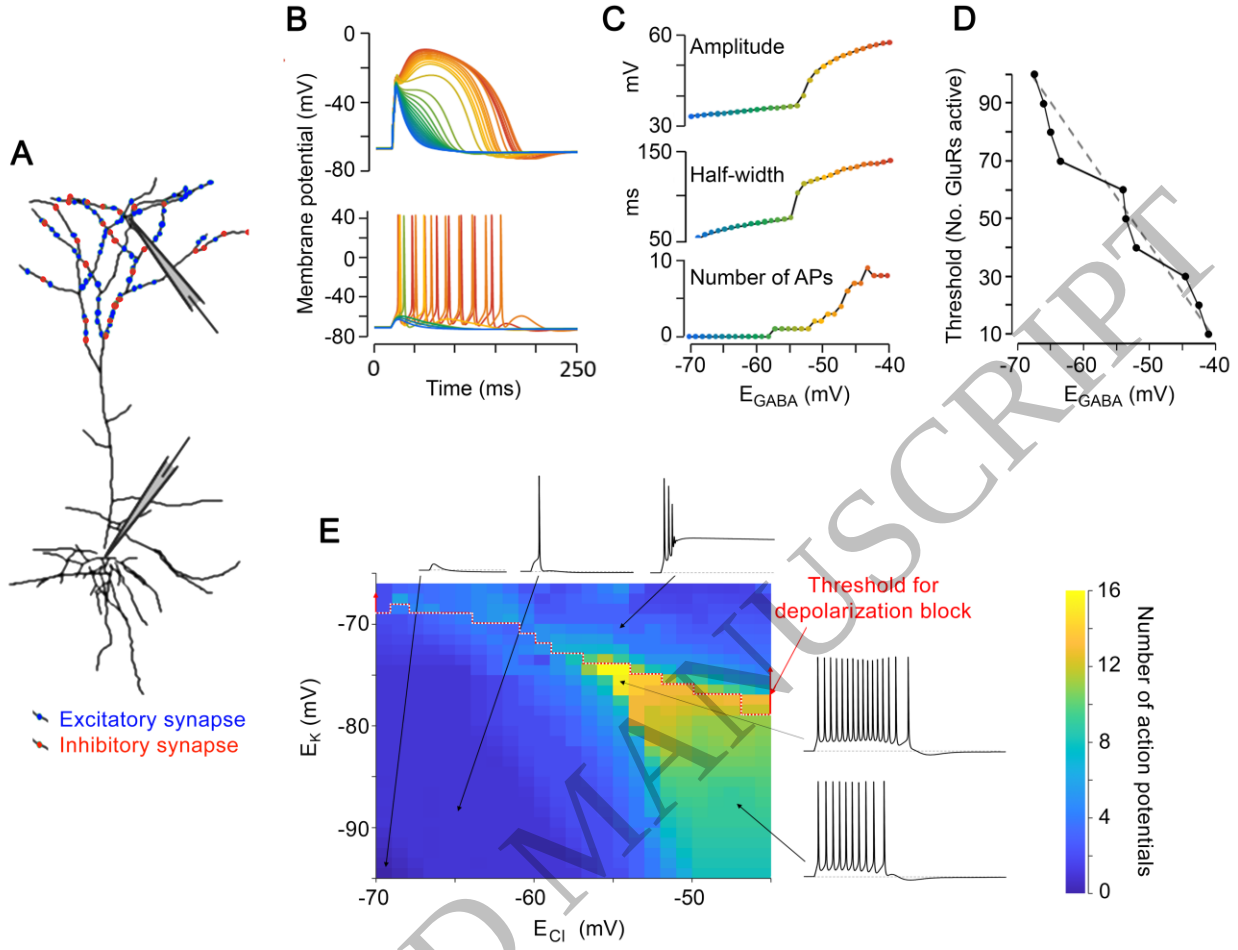

Figure 8
165x125 mm (5.4 x DPI)